



Understanding the catalytic ozonation process on ceria nanorods: Efficacy, Frenkel-type oxygen vacancy as a key descriptor and mechanism insight

Lei Wu, Jiaren Wang, Chenyu Yang, Xingmin Gao, Yan Fang, Xiaoning Wang^{*},
Winston Duo Wu^{*}, Zhangxiong Wu^{*}

Particle Engineering Laboratory, School of Chemical and Environmental Engineering, College of Chemistry, Chemical Engineering and Materials Science, Soochow University, Suzhou, Jiangsu 215123, PR China

ARTICLE INFO

Keywords:

Catalytic ozonation
Ceria nanorods
Frenkel-type oxygen vacancy
Mechanism
Water treatment

ABSTRACT

This work investigated property-activity correlations of ceria (CeO_2) in heterogeneous catalytic ozonation (HCO) and explored the key descriptor from various properties. CeO_2 nanorods (NRs) calcined at 300–700 °C were adopted in HCO for degrading three organic pollutants. With their physicochemical properties characterized and their HCO performances analyzed in detail, the correlations between different properties and the rates of O_3 decomposition, pollutant degradation and total organic carbon (TOC) removal were revealed. Fast pollutant degradation, high TOC removal, good stability and wide pH applicability were achieved. Linear relationships between the rates of O_3 decomposition/TOC removal and the density of Frenkel-type oxygen vacancy (OV) were established. Theoretical and spectroscopic studies revealed OV could boost O_3 decomposition to generate reactive oxygen species (ROS). The mechanism for ROS generation and pollutant degradation was proposed. This study would contribute to designing efficient catalysts and understanding their performances in HCO for abatement of organic pollutants in wastewaters.

1. Introduction

Transition metal oxides (TMOs) are being widely explored in heterogeneous catalytic ozonation (HCO) for wastewater treatment [1–3]. In recent years, not only a series of TMOs, such as MnO_2 , Fe_2O_3 and CeO_2 single oxides [4–6], LaMO_3 ($\text{M} = \text{Mn, Fe}$) and MgM_xO_y ($\text{M} = \text{Mn, Fe}$) binary oxides and Ce-Ti-Zr multi-component oxides [7–9], with excellent HCO performances have been reported, but also enhanced understanding of the reaction mechanisms has been progressively achieved [5, 7, 10, 11]. Nevertheless, in gas-liquid-solid three-phase HCO processes, the multiple material property parameters of TMOs, such as surface area, crystal plane exposure, metal valence, surface hydroxyl (OH), oxygen vacancy (OV) and acid-base sites, often result in complicated influences on ozone (O_3) adsorption and activation, pollutant adsorption and formation of reactive oxygen species (ROS), subsequently leading to complicated influences on performance [5, 7, 10, 12–14]. This issue greatly hinders identification of key active sites and makes it difficult to establish clear property-activity correlations. Therefore, it is important to identify key descriptors for evaluating the performances of TMOs in HCO.

Among various TMOs, rare-earth CeO_2 is promising in HCO because of its tunable nanoscale morphologies, high $\text{Ce}^{4+}/\text{Ce}^{3+}$ redox activity, excellent stability, low toxicity and high abundance. In addition, it possesses rich OV sites, which may play important roles in redox reactions. An intrinsic OV and two neighboring Ce^{3+} can be formed by removing an oxygen atom from the CeO_2 lattice [15]. A Frenkel-type OV can be generated by moving an oxygen atom from its lattice site to an interstitial site [16]. Recent works have shown CeO_2 can be used in HCO for efficient degradation of various organic pollutants [5, 8, 17–19]. However, a couple of critical issues require further investigation. First, it is puzzling that CeO_2 materials prepared using different methods exhibited different HCO performances. For example, Zhang et al. reported the oxalate removal in a O_3/CeO_2 system was approximately the sum of that removed by ozonation alone and that removed by CeO_2 adsorption alone [20]. This means the adopted CeO_2 material has no obvious activity in HCO for oxalate degradation. However, Feng et al. reported that rod-like CeO_2 was capable of removing 80% oxalic acid in HCO [21], suggesting a high catalytic activity. Second, the complicated correlations among different properties of CeO_2 and the sophisticated interplay between these properties and the HCO performances make it

^{*} Corresponding authors.

E-mail addresses: wangxiaoning@suda.edu.cn (X. Wang), duo.wu@suda.edu.cn (W.D. Wu), zhangwu@suda.edu.cn (Z. Wu).

<https://doi.org/10.1016/j.apcatb.2022.122152>

Received 9 August 2022; Received in revised form 31 October 2022; Accepted 8 November 2022

Available online 11 November 2022

0926-3373/© 2022 Elsevier B.V. All rights reserved.

hard to identify and understand the key factor determining the performance. Pinheiro da Silva et al. prepared three CeO₂ samples from different cerium citrate-based precursors and adopted them in HCO for degrading phenol [22]. The CeO₂ sample with the lowest surface area but the highest surface Ce³⁺ percentage showed the best total organic carbon (TOC) removal efficiency. Very differently, in the work of Zhang et al. [19], the surface area of the mesoporous CeO₂ prepared with microcrystalline cellulose as the template was 5.5 times higher than that of the sample prepared without using template, but the percentage of Ce³⁺ of the former sample (16.81%) was much lower than the latter (29.52%). By using them in HCO for phenol degradation, the former sample showed both higher phenol and chemical oxygen demand (COD) removal rates than the latter. Obviously, the roles and importance of the surface area and Ce³⁺ percentage of the CeO₂ materials are different in these studies in spite of the same application. In the recent work by Afzal et al. [5], CeO₂ nanorod, nanocube and nanooctahedron were used in HCO for degradation of p-nitrophenol. Through the detailed investigation, they concluded the basic site, Ce³⁺, Frenkel-type OV and coordination number of surface atoms on different crystal facet of CeO₂ were the major factors influencing performance. It was found that high concentrations of Ce³⁺, Frenkel-type OV and basic site and the nanorod morphology were preferred for better performance. However, it has not been clarified how these different influencing factors of CeO₂ are linked. It is also unclear which factor is the key one and how it influences O₃ activation on CeO₂.

The main object of this work is to identify the critical descriptor for evaluating the HCO performance of CeO₂ and to understand its key role in activation of O₃. CeO₂ nanorods (CeO₂-NR) were subject to thermal treatment at 300–700 °C to regulate their properties. Their surface area, crystal size, Ce³⁺ percentage, and concentrations of surface OH, Frenkel-type OV and acid-base sites were carefully characterized. These properties were found to be closely linked one another and their correlations were studied. Their performances in HCO for degradation of three typical pollutants were evaluated and the relationships between their properties and performances were explored. It was found that Frenkel-type OV could be used as the key descriptor to link the concentrations of surface OH and acid-base sites of the CeO₂-NR samples and to linearly correlate with their activities in O₃ decomposition and TOC removal. Theoretical calculations and spectroscopic studies revealed OV could greatly enhance O₃ activation on both the surface Ce and OH sites of CeO₂-NR.

2. Experimental section

2.1. Preparation and characterization of CeO₂ nanorods

The details of the used chemicals were provided in the [Supporting Information](#). The CeO₂ nanorods (NRs) were synthesized by a hydrothermal method [23]. Typically, 1.30 g of Ce(NO₃)₃•6H₂O and 14.40 g of NaOH were dissolved in 20 and 40 mL of water, respectively. The two solutions were mixed in a 100 mL Teflon bottle and stirred for 30 min. Next, the Teflon bottle was sealed in a stainless-steel autoclave and heated at 100 °C for 24 h. The obtained precipitate was separated by centrifugation at 9000 rpm for 8 min and washed by water and ethanol until a neutral pH was achieved in the filtrate. It should be noted that the remained Na content in the precipitate was negligible based on elemental analysis. The precipitate was dried at 60 °C overnight and calcined at various temperatures (300–700 °C with a gap of 100 °C) for 3 h. The final samples were labeled as CeO₂-NR-T, wherein T stands for the calcination temperature in °C.

The obtained samples were characterized using a series of techniques. The details were provided in the [Supporting Information](#).

2.2. Catalytic ozonation

The experimental set-up for catalytic ozonation was shown in [Fig. S1](#).

O₃ was produced from O₂ using an O₃ generator (Anseros Ozomat COM). The degradation of three representative pollutants, phenol, carbamazepine (CBZ) and oxalate, was evaluated. Typically, 112 mL of a phenol solution (100 mg/L) and 0.28 g of a CeO₂ catalyst were stirred at 25 °C for 30 min to reach adsorption equilibrium. Then, a mixed O₂/O₃ gas (18 mL/min) with an O₃ concentration of 50 mg/L was continuously bubbled into the bottom of the flask thorough a porous glass aerator with a pore size of 10–15 μm. The O₃ dose rate was about 0.9 mg/min. The use of excessive O₃ was mainly because of the low solubility of O₃ in aqueous solution and the short residence time of bubbling O₃ in batch solutions. At various time intervals, 4.0 mL of the mixture was withdrawn and separated through a polytetrafluoroethylene (PTFE) filter. At each time interval, 0.5 mL of the filtrate was immediately added into a brown injection bottle (1.5 mL) containing 0.5 mL of a Na₂S₂O₃ solution (0.1 mol/L) to remove the residual O₃ and other ROS. Then, the remained phenol concentration was determined using high performance liquid chromatography (HPLC, Agilent Technologies 1260 Infinity) equipped with a diode array detector. The experiment of single ozonation (without catalyst) was carried out under the same conditions. The TOC content was analyzed using a TOC analyzer (TOC-L CPHCN200, Shimadzu).

The O₃ decomposition rate on different catalysts was determined. Specifically, 0.28 g of a CeO₂ catalyst was added into 250 mL of an O₃-saturated solution. The suspension was stirred at 25 °C. At given time intervals, 2.0 mL of the suspension was withdrawn and the catalyst was separated by a PTFE filter. The supernatant was added into 5.0 mL of an indigo solution. The resulted solution was analyzed using a UV–vis spectrophotometer (DR-6000, HACH) at 610 nm to determine the O₃ concentration with a pre-determined standard curve ([Fig. S2](#)). The O₃ self-decomposition rate (without catalyst) of the O₃-saturated solution was also measured.

2.3. ROS quenching and detection experiments

To check the types of ROS generated during the HCO process, in separate experimental sets, quenching agents, including tert-butanol (TBA) (100 mM), *p*-benzoquinone (*p*-BQ) (12 mM) or furfural alcohol (FFA) (12 mM), were added to the suspension to evaluate the changes of degradation performance.

The electron spin resonance (ESR) technique was also employed to detect •OH and •O₂ using 5, 5-dimethyl-1-pyrroline N-oxide (DMPO) (250 mM) and ¹O₂ using 2, 2, 6, 6-tetramethyl-4-piperidinol (TEMP) (100 mM). For detection of •OH and ¹O₂, the reaction was conducted in aqueous solution. For detection of •O₂, methanol was adopted as solvent. Specifically, the O₃ stock solution was prepared by continuously bubbling a mixed O₂/O₃ gas into deionized water or methanol. Meanwhile, 10 mg of CeO₂-NR-300 and 200 μL of the DMPO or TEMP solution were mixed to form a suspension. Then, 1 mL of the O₃ stock solution was added into the suspension and promptly mixed. A certain volume of the mixture was injected into a capillary tube and then the ESR spectrum was collected at ambient temperature on a JES-X320 spectrometer under the following operating conditions: a modulation frequency of 100 kHz, a sweep width of 0.5 mT, a microwave power of 1 mW, a microwave frequency of 9.15 GHz and a centerfield of 326.0 ± 5 mT.

2.4. Density function theory calculation

In the slab model of CeO₂, a 2 × 3 supercell of four atomic layers was adopted. The bottom two layers of atoms were fixed in their optimized bulk positions, while the top two layers and the adsorbate were allowed to fully relax. The first principle density function theory (DFT) calculations were performed using the Vienna Ab initio Simulation Package (VASP) and the projector augmented wave (PAW) method [24,25]. The exchange-functional was treated using the generalized gradient approximation (GGA) of Perdew-Burke-Ernzerhof (PBE) functional [26]. According to the previous study [27], the optPBE method was employed

to consider the van der Waals interaction due to its accuracy in describing both electronic and structural properties. The energy cutoff for the plane wave basis expansion was set to 450 eV and the force on each atom less than 0.02 eV/Å was set for convergence criterion of geometry relaxation. A 15 Å vacuum was added along the z direction in order to avoid the interaction between periodic structures. The Brillouin zone integration was performed using $3 \times 3 \times 1$ k-point sampling. The self-consistent calculations applied a convergence energy threshold of 10^{-4} eV. A Hubbard- U term using the Liechtenstein approach was used to account for self-interaction effects, which are particularly significant for the localized Ce (4 f) orbitals with $U-J = 4.5$ eV [28]. The adsorption energy (E_{ads}) of O_3 was calculated according to Eq. (1), wherein E_{total} is the total energy of the O_3 adsorbed on the CeO_2 substrate, E_{mol} and E_{sub} are the energies of the isolated O_3 molecule and the CeO_2 substrate, respectively.

$$E_{\text{ads}} = E_{\text{total}} - E_{\text{mol}} - E_{\text{sub}} \quad (1)$$

3. Results and discussion

3.1. Structural and chemical properties of CeO_2 -NR in dry state

X-ray diffraction (XRD) patterns of CeO_2 -NR-T show the characteristic peaks of a pure fluorite-type cubic structure (PDF #75-0151) (Fig. 1a). As the temperature increases, the crystallite size increases slightly (11.2–12.1 nm) at 300–500 °C and more rapidly (13.6–17.0 nm) at 600–700 °C (Table 1). The surface areas (77–90 m^2/g) and pore volumes (0.60–0.71 cm^3/g) of the samples obtained at 300–500 °C are close, but dramatically decrease to $\leq 3 \text{ m}^2/\text{g}$ and $\leq 0.05 \text{ cm}^3/\text{g}$ at 600–700 °C (Fig. 1b and Table 1), confirming severe sintering occurs at ≥ 600 °C. All the samples are made of nanorods. Their diameter and length are similar at 300–500 °C and increase to some extent at 600–700 °C (Fig. 2a–e). Typically, the nanorods in CeO_2 -NR-300 have a diameter of 8–10 nm and a length of 40–120 nm, and they mainly expose the (110) facet. The observed lattice fringes with a spacing of 0.19 nm can be indexed to the (220) or (110) plane (Fig. 2f).

The Ce 3d X-ray photoelectron spectroscopy (XPS) spectra of CeO_2 -NR-T can be deconvoluted into eight peaks, which are categorized into two groups of spin orbitals (Fig. 3a). The peaks labeled with u ($u-u''$) and v ($v-v''$) correspond to $3d_{3/2}$ and $3d_{5/2}$, respectively. The u' (902.43 eV) and v' (884.23 eV) peaks are assigned to Ce^{3+} , and the other six peaks to Ce^{4+} . The ESR spectra of CeO_2 -NR-T show the characteristic g_{\perp} and g_{\parallel} signals with similar peak intensities (Fig. S3), confirming the presence of paramagnetic Ce^{3+} [29]. The similar peak intensity in the

Table 1

Summary of the physicochemical properties of CeO_2 -NR-T.

Sample	D ^a (nm)	S _{BET} ^b (m^2/g)	V _t ^c (cm^3/g)	Ce ³⁺ ^d (%)	O _{OH} ^e (%)	OH(a) ^f (mmol/g)
CeO ₂ -NR-300	11.2	82	0.60	19.90	36.44	0.095
CeO ₂ -NR-400	11.6	90	0.71	19.73	29.91	0.090
CeO ₂ -NR-500	12.1	77	0.66	18.89	28.12	0.080
CeO ₂ -NR-600	13.6	3	0.05	19.49	25.70	0.060
CeO ₂ -NR-700	17.0	1	0.04	17.59	24.70	0.030

^a Crystallite size calculated using the Scherrer equation based on the (111) diffraction

^b Specific surface area calculated using the Barrett-Emmett-Teller method

^c Total pore volume calculated from the N_2 adsorbed amount at P/P_0 of 0.99

^d Ce³⁺% value calculated from the Ce 3d XPS spectra

^e O_{OH}% value calculated from the O 1s XPS spectra

^f Density of acidic hydroxyl measured by the titration method

ESR spectra of these samples indicates the Ce^{3+} contents in their bulk structure are similar. The relative percentage of Ce^{3+} ($\text{Ce}^{3+}\%$) on their surface can be calculated using the integrated peak areas (A) of the Ce 3d XPS spectra based on Eq. (2) [30].

$$\text{Ce}^{3+}\% = \frac{A_{u'} + A_{v'}}{A_u + A_{u'} + A_v + A_{v'} + A_{u''} + A_{v''} + A_{u'''} + A_{v'''}} \quad (2)$$

The $\text{Ce}^{3+}\%$ value of the samples calcined at 300–600 °C is close (18.9–19.9%), and it only gently decreases to 17.6% at 700 °C (Table 1), indicating the $\text{Ce}^{3+}/\text{Ce}^{4+}$ ratio of the samples is thermally stable, which can also be indicated by the similar peak intensity of their ESR spectra (Fig. S3). In the O 1s XPS spectra (Fig. 3b), the peak centered at 529.4 eV is assigned to the lattice oxygen (O_{lat}) of CeO_2 , and that centered at 531.4 eV to the surface OH (O_{OH}) associated with OV [31,32]. The relative percentage of O_{OH} ($\text{O}_{\text{OH}}\%$) decreases gradually (36.4–24.7%) with the increase of temperature (Table 1), because of gradual elimination of OH at higher temperatures via the reaction shown in Eq. (3) [33,34]. This can be verified by the in-situ attenuated total reflection Fourier transform Infrared (ATR-FTIR) spectra (Fig. 3c). There are three types of OH in CeO_2 -NR-300, including terminal ($3694\text{--}3732 \text{ cm}^{-1}$), bridged ($3625\text{--}3662 \text{ cm}^{-1}$) and multi-coordinated ($3500\text{--}3600 \text{ cm}^{-1}$) OH [35,36]. As the temperature increases, the terminal OH can be completely eliminated and the other two types are gradually reduced.

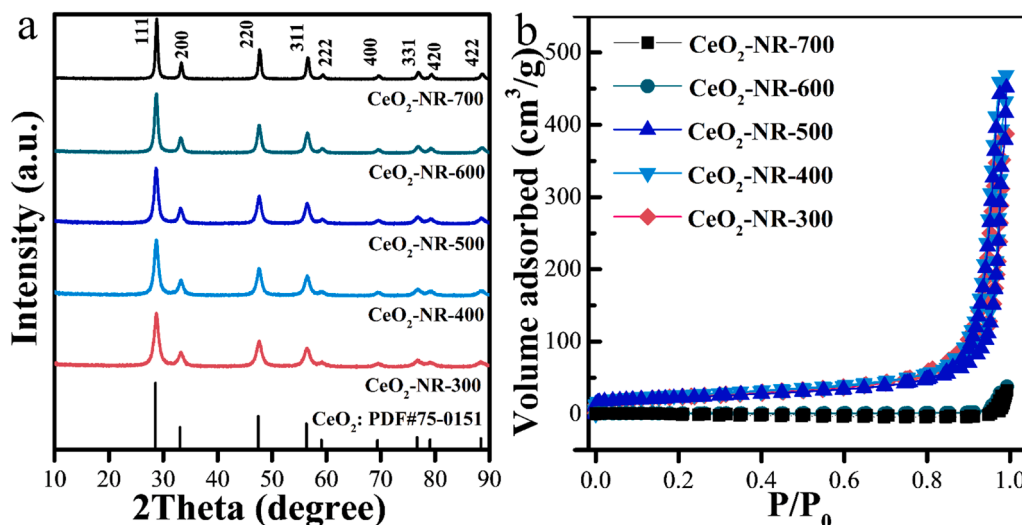


Fig. 1. XRD patterns (a) and N_2 sorption isotherms (b) of CeO_2 -NR-T.

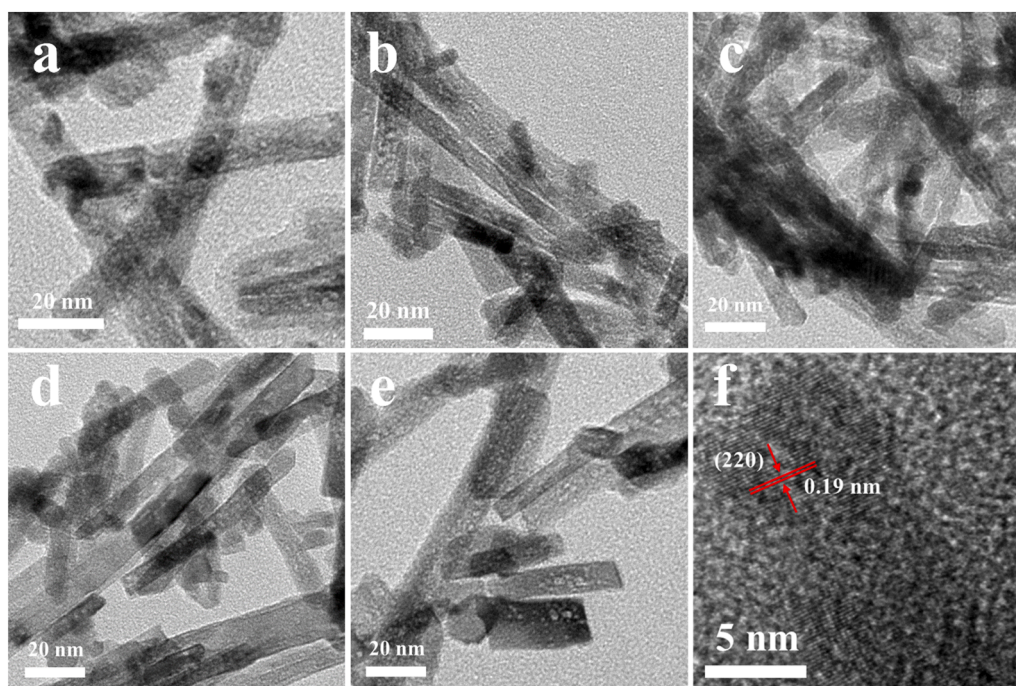
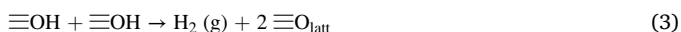


Fig. 2. TEM (a-e) and HRTEM (f) images of CeO₂-NR-300 (a, f), CeO₂-NR-400 (b), CeO₂-NR-500 (c), CeO₂-NR-600 (d) and CeO₂-NR-700 (e), respectively.



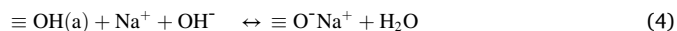
In the Raman spectra of CeO₂-NR-T, the strong band at about 460 cm⁻¹ is ascribed to the symmetric breathing vibration of the tetrahedrally coordinated oxygen ions about the unit cell center (F_{2g} band) (Fig. 4a) [37]. The minor band at about 600 cm⁻¹ (D band) is attributed to the presence of Frenkel-type OV (Fig. 4b) [38,39]. The Frenkel-type OV in CeO₂ is sensitive to its surface structure [39], while the Ce³⁺ signal in the ESR spectra reflects more bulk structure information. Resultantly, different from the similar peak intensity in the ESR spectra of CeO₂-NR-T (Fig. S3), the signal intensity of the D band in the Raman spectra of these samples decreases gradually with the increase of temperature (Fig. 4b). The concentration of Frenkel-type OV in CeO₂ can be semi-quantitatively analyzed using the I_D/I_{F2g} ratio derived from the peak intensities of the two bands [39]. As shown in Fig. 4c, the I_D/I_{F2g} value decreases linearly with the increase of temperature. This result indicates the concentration of Frenkel-type OV in CeO₂-NR-T decreases linearly as the temperature increases, because it can be gradually eliminated at higher temperatures, in accordance with the O 1s XPS results.

The Ce³⁺ and OV sites in CeO₂-NR-T are linked with their acid-base sites. This can be depicted by the NH₃- and CO₂-temperature programmed desorption (TPD) profiles. CeO₂-NR-300 shows three pairs of acid-base sites. Each acid-base pair is located at almost the same desorption temperature, namely, a weak pair at about 150 °C, a medium one at about 260 °C and a strong one at about 410 °C (Fig. 5a, b). In addition, the densities of the acid-base sites are very close (Fig. 5c). The same trends can also be observed for the other CeO₂-NR-T. As the temperature increases, the density of each pair of acid-base sites gradually decreases (Fig. 5c), because of the higher temperature causing enhanced sintering and loss of surface oxygen species. Interestingly, the plots of the acid-base site densities in CeO₂-NR-T against the I_D/I_{F2g} values show much better linearity compared with those against the specific surface area values (Fig. S4). Therefore, the Frenkel-type OV in CeO₂-NR-T might be used as an indicator for their densities of acid-base sites [5,40], and these properties can be simply regulated by temperature.

3.2. Surface OH of CeO₂-NR in wet state

In HCO processes using TMOs, surface OH plays an important role in O₃ activation [12,13,41]. The surface OH of CeO₂-NR-T in dry state could be very different from that in wet state. When contacted with water, the Ce³⁺ and OV sites can promote the dissociation of chemisorbed water to form more surface OH [42]. In the in-situ FTIR spectra (Fig. 3c), by exposing the sample in-situ treated at 500 °C in water vapor, the terminal OH can be re-generated and the other types of OH can be recovered to a large extent. Additionally, intensive signals (3400–3100 cm⁻¹) from hydrogen-bonded OH can also be observed.

According to literature [43], titration using NaOH solutions can quantify the concentration of acidic OH, OH(a), according to Eq. (4). After dispersed in water, the measured density of OH(a) in CeO₂-NR-T is 0.095–0.030 mmol/g (Fig. S5 and Table 1). With the increase of temperature, the OH(a) density gradually decreases, especially for the samples obtained at 600–700 °C showing much sharper decreases. Because the Ce³⁺% values for CeO₂-NR-T are very close, the sharp decrease of the OH(a) density at 600–700 °C is mainly because of the severe sintering causing loss of surface area and elimination of OV. In addition, according to the NH₃- and CO₂-TPD results and the principle of charge balance [44], the acid-base sites in a CeO₂ sample could be equal. Hence, CeO₂-NR-T should possess the similarly amounts of basic OH and the same temperature dependence could be expected. It should be pointed out that the density of OH(a) of CeO₂-NR-T in water is also proportional to the relative concentration of their Frenkel-type OV (Fig. S6), further indicating Frenkel-type OV might be used as a simple indicator for the OH density of CeO₂-NR-T.



3.3. Performances of CeO₂-NR in catalytic ozonation

To evaluate the performances of CeO₂-NR-T in HCO for phenol degradation, adsorption, single ozonation and catalytic ozonation were compared. Adsorption of phenol on CeO₂-NR-T is very low (Fig. 6a and S7a, b), indicating phenol degradation is determined by ozonation. Single ozonation can degrade 92% phenol in 60 min. Catalytic

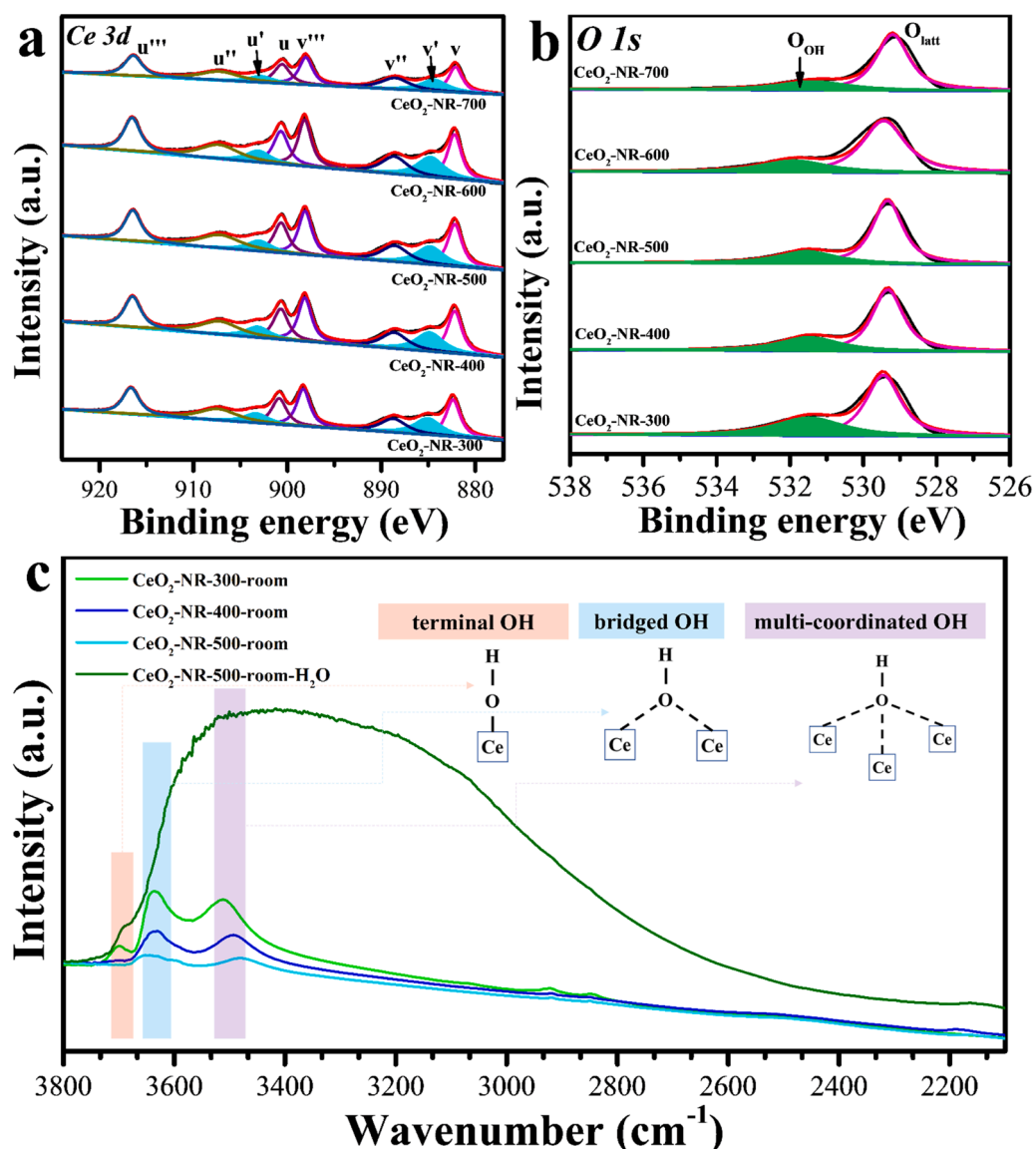


Fig. 3. $\text{Ce } 3d$ (a) and $\text{O } 1s$ (b) XPS, and in-situ ATR-FTIR (c) spectra of $\text{CeO}_2\text{-NR-T}$. The words “-room” and “- H_2O ” in (c) indicate the spectra were recorded at room temperature (after the heat treatment) and then exposed to water vapor, respectively.

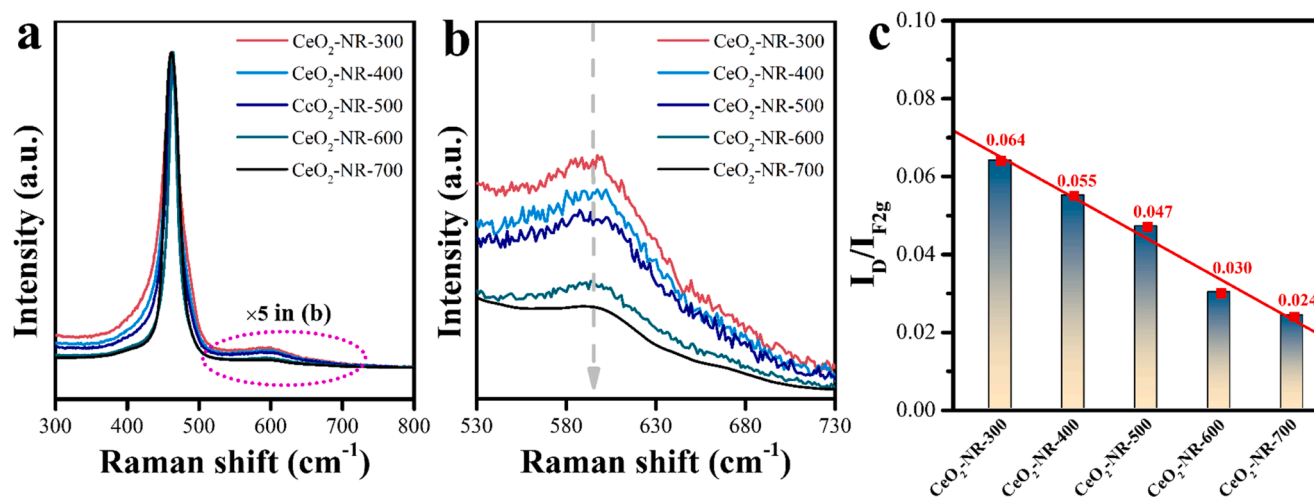


Fig. 4. Raman spectra (a), the magnified spectra (b) and the relative Frenkel-type OV concentration chart (c) of $\text{CeO}_2\text{-NR-T}$, respectively.

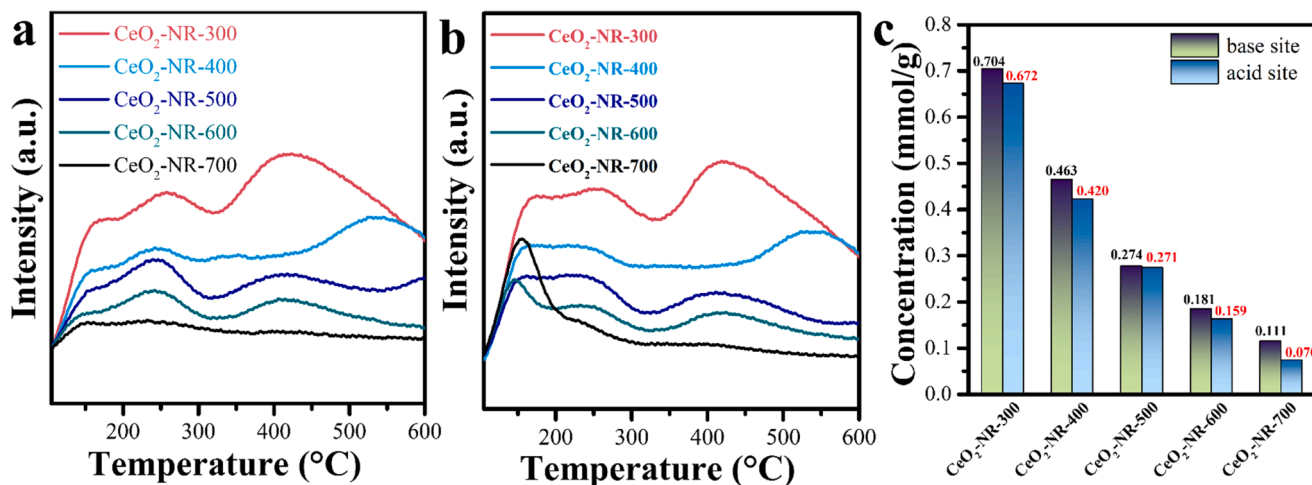


Fig. 5. NH₃-TPD (a), CO₂-TPD (b) profiles and the corresponding acid-base site concentration chart (c) of CeO₂-NR-T.

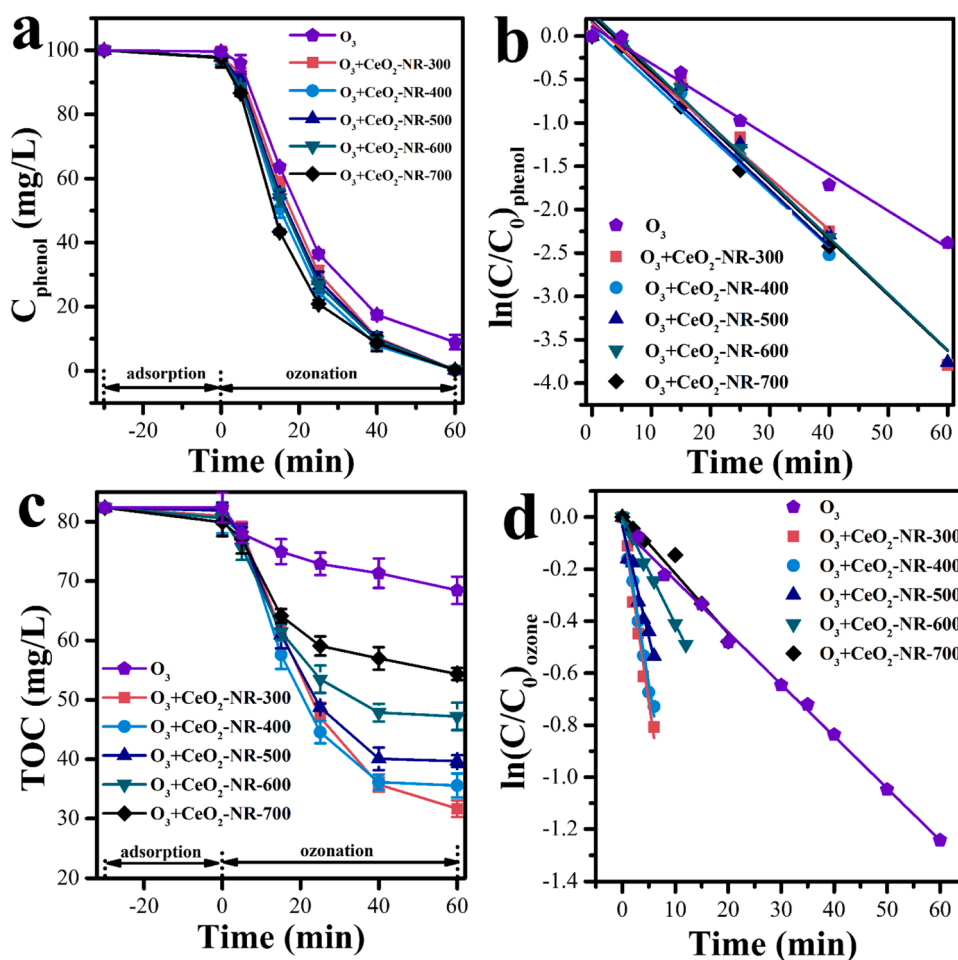


Fig. 6. The time-dependent phenol degradation curves (a), the fitting curves for the degradation kinetics (b) and the corresponding TOC removal curves (c) for single ozonation and catalytic ozonation on CeO₂-NR-T, and the fitting curves for the kinetics of O₃ self-decomposition and catalytic decomposition on CeO₂-NR-T (d). Experimental conditions in (a-c): initial pH 6.4, catalyst dosage 2.5 g/L (if used), gaseous [O₃] 50 mg/L, flow rate 18 mL/min.

ozonation by CeO₂-NR-300 shows nearly 100% phenol degradation in 60 min (Fig. 6a), which is improved to some extent compared with that of single ozonation. Both single and catalytic ozonation follow the apparent first-order reaction kinetics, and their rate constant, $k_{app-phenol}$, is -0.042 and -0.065 min⁻¹, respectively (Fig. 6b). The phenol degradation rates by catalytic ozonation on CeO₂-NR-T are very close (Fig. 6a,

b and Table S1). The above results indicate phenol degradation is mainly proceeded in bulk solution via direct oxidation by O₃, in accordance with the previous work [22]. The presence of CeO₂ shows positive influence on the kinetics of phenol oxidation because of the powerful ROS generated from activation of O₃ on the catalyst surface, but the influence is not remarkable because of the much lower concentration of ROS than

that of O_3 .

Compared with the similar phenol degradation performance, the difference in TOC removal rate by single and catalytic ozonation is huge (Fig. 6c). Single ozonation only removes 16.9% of TOC in 60 min, while a much higher TOC removal (61.5%) can be achieved by catalytic ozonation on CeO_2 -NR-300. At this point, the utilization rate of O_3 on CeO_2 -NR-300 was roughly estimated to about 78% by simply assuming phenol could be completely converted to oxalic acid by O_3 and then the mineralization of oxalic acid would depend on the $\bullet OH$ generated from O_3 . The TOC removal on all the CeO_2 -NR-T is much higher than that of single ozonation, but gradually decreases from 61.5% to 34% at 60 min as the temperature increases (Fig. 6c and Table S1). Meanwhile, the TOC removal rates on CeO_2 -NR-T become much slower at 40–60 min compared with the initial rates. This is mainly because most phenol and a large fraction of the intermediates are removed in 40 min. The decreased reactant concentrations and the remained refractory intermediates lead to the slowed TOC removal rates. In addition, the adsorption amounts of the common intermediates, such as oxalic acid and oxalate commonly produced in catalytic ozonation of phenol [45], on CeO_2 -NR-300 are nearly zero (Fig. S7c, d). The above results indicate the intermediates from phenol oxidation is difficult to be further oxidized by O_3 [45]. Deep oxidation of these intermediates depends on the capability of CeO_2 -NR-T in activating O_3 to generate more powerful ROS.

To evaluate the capability of CeO_2 -NR-T in activating O_3 , the kinetics of aqueous O_3 decomposition with or without catalyst was compared. Both O_3 self-decomposition and catalytic decomposition follow the first-order reaction kinetics (Fig. 6d). According to Eq. (5) [46], the apparent rate constant for self-decomposition (k_{O_3}) is -0.021 min^{-1} . Based on Eqs. (6) and (7) [46], the apparent rate constant for catalytic decomposition ($k_{O_3\text{-cata}}$) dramatically increases (Fig. 6d and Table S1). Typically, the $k_{O_3\text{-cata}}$ (-0.140 min^{-1}) for CeO_2 -NR-300 is about 6.7 times of k_{O_3} . As the temperature increases, $k_{O_3\text{-cata}}$ for CeO_2 -NR-T decreases gradually, the same trend as that of the TOC removal. Therefore, the activation of O_3 at the surface of CeO_2 -NR-T is a critical step to generate powerful ROS for deep oxidation of the intermediates. The different active site density of CeO_2 -NR-T determines their different TOC removal rate.

$$-\frac{d[O_3]}{dt} = k_{O_3}[O_3] \quad (5)$$

$$-\frac{d[O_3]}{dt} = k_{\text{cata}}[O_3][\text{active sites}] \quad (6)$$

$$-\frac{d[O_3]}{dt} = k_{O_3\text{-cata}}[O_3] \quad (7)$$

Next, the influence of pH on the performance of CeO_2 -NR-300 was studied because the surface OH is linked with the performance and pH determines its charge state [1,2]. High performance (fast phenol degradation and high TOC removal) can be achieved at pH of 3.5–12.0 (Fig. 7), indicating the applicability of CeO_2 -NR-300 in a wide pH range. Nevertheless, interesting differences can be observed at different pH values. The phenol degradation rates under both acidic (pH=3.5) and basic (pH=8.9 and 12.0) conditions are more or less accelerated compared with that at pH=6.4 (natural pH of the phenol solution) (Fig. 7a). However, the trend of TOC removal at different pH values is different (Fig. 7b). The TOC removal is the best at pH=8.9, and it becomes inferior at all the other studied pH values. The fastened phenol degradation under basic conditions is mainly because OH^- is an initiator for O_3 decomposition [47]. On the contrary, the poorest TOC removal can be explained by two factors. First, the pH_{pzc} (point of zero charge) of CeO_2 -NR-300 is about 8.9 (Fig. S8). At pH=12.0, the negatively charged surface is undesirable for adsorption of negatively charged intermediates (such as oxalate). Second, deprotonated OH^- becomes less active for O_3 activation to generate ROS, which is decisive for TOC removal [1,2]. On the other hand, the slightly enhanced phenol degradation at pH=3.5 is probably due to the high total O_3 exposure (longer lifetime for O_3 under acidic conditions) [47]. However, the declined TOC removal compared with that at pH of 6.4 is probably because the unfavored adsorption of intermediates and the less active protonated OH ($-OH_2^+$) for O_3 activation. Therefore, the best TOC removal at a pH equal to pH_{pzc} indicates the key role of OH in activating O_3 .

Furthermore, the stability of CeO_2 -NR-300 in HCO was evaluated. The phenol degradation performance keeps the same after four consecutive runs (Fig. 8a). This is because phenol is mainly oxidized by O_3 in bulk solution. The TOC removal also maintains at a high level and declines gently at the fourth cycle (Fig. 8b). Because the adsorption capacities of phenol, oxalic acid and oxalate on CeO_2 -NR-300 are very low (Fig. S7), the coordination between CeO_2 and phenol or its intermediates should not be the main reason to the slight decline of TOC removal during recycling. The slight decline is more likely to be caused by the change of catalyst surface property [5,48]. XPS spectra show after four cyclic runs, the $Ce^{3+}\%$ and $OH\%$ values gently decrease from

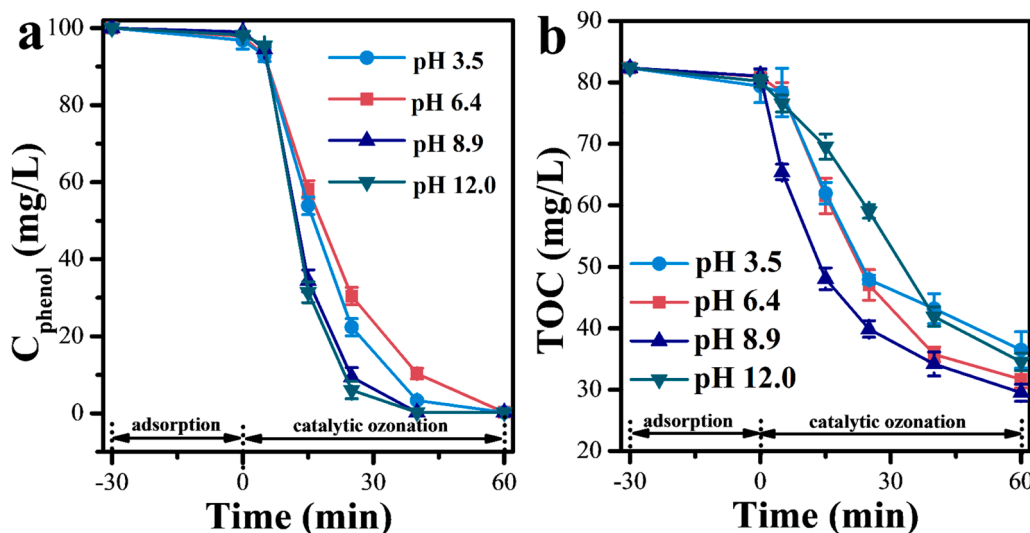


Fig. 7. Effects of the initial pH values on the phenol degradation (a) and TOC removal (b) for catalytic ozonation of phenol on CeO_2 -NR-300. Experimental conditions: gaseous $[O_3]$ 50 mg/L, flow rate 18 mL/min, catalyst dosage 2.5 g/L.

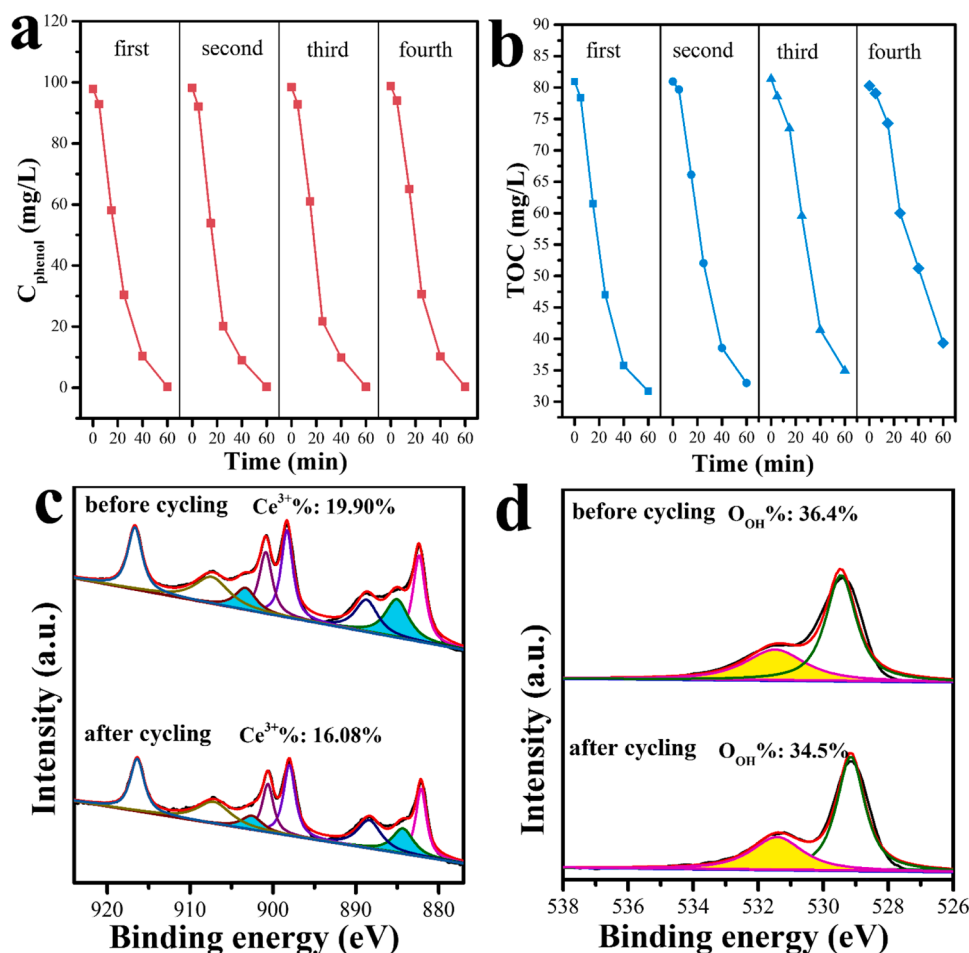


Fig. 8. The phenol degradation (a) and TOC removal (b) during the catalytic ozonation of phenol on CeO₂-NR-300 for four consecutive cycles, and the Ce 3d (c) and O 1s (d) XPS spectra of CeO₂-NR-300 before and after the four cycles of reaction.

19.8% to 16.1% and from 36.4% to 34.5% (Fig. 8c, d), respectively, indicating a high stability. This result is different from the previous work on using CeO₂ for degradation of p-nitrophenol, which showed a more obvious decrease of Ce³⁺ and an increase of O_{OH}% after the HCO process [5]. Because the Ce³⁺ and OH sites are closely related with O₃ activation, their gentle declines account for the slight decrease in TOC removal at the fourth cycle.

In addition, the degradation performances toward other two representative pollutants via HCO on CeO₂-NR-T were evaluated. In treating CBZ (50 mg/L), a typical example of pharmaceuticals and personal care products causing worldwide concerns, CeO₂-NR-300 shows a very fast degradation rate (slightly better than single ozonation) and excellent TOC removal (much better than single ozonation) (Fig. S9). In treating oxalate ions (100 mg/L), CeO₂-NR-300 shows good degradation performance (50% TOC removal in 60 min). Similarly, the performances of CeO₂-NR-T in degradation both CBZ and oxalate decline with the increase of temperature. CeO₂-NR-300 is potentially a general catalyst in HCO for degrading different organic pollutants.

3.4. Identification of ROS

The ROS involved in the HCO process was analyzed by ESR. To detect •OH and •O₂⁻, DMPO was employed as the spin-trapping agent [49,50]. Meanwhile, TEMP was utilized to detect ¹O₂ [50]. In the O₃/CeO₂-NR-300/DMPO/water mixture, signals with an intensity ratio of 1: 2: 2: 1 from the DMPO-•OH adduct can be observed, and in the O₃/CeO₂-NR-300/DMPO/methanol mixture, characteristic sextet signals assigned to the DMPO-•O₂⁻ adduct can be identified (Fig. 9a) [49].

In the O₃/CeO₂-NR-300/TEMP/water mixture, characteristic triplet signals for the TEMP-¹O₂ adduct are present (Fig. 9a) [50]. Without catalyst, in the O₃/DMPO/water, O₃/DMPO/methanol and O₃/TEMP/water mixtures, much weaker (almost invisible) signals are present (Fig. 9b) [51,52]. The results reveal CeO₂-NR-300 can significantly promote the production of •OH, •O₂⁻ and ¹O₂ in the HCO process.

Next, the contribution of different ROS to the degradation was discussed. The oxidation potentials of O₃ (up to 2.07 eV), •OH (up to 2.8 eV), •O₂⁻ (up to 2.4 eV) and ¹O₂ (up to 2.2 eV) determine their oxidation capability [1,2,53]. The ¹O₂ pathway depends on electron transfer between adsorbed surface complexes [2]. Considering the relatively low oxidation potential of ¹O₂ and the facts that adsorption of either phenol or its typical intermediates on CeO₂-NR-300 is limited (Fig. S7) and phenol is mainly oxidized by O₃ but with a poor TOC removal (Fig. 6a, c), the contribution of ¹O₂ in both phenol degradation and TOC removal should be minimal. Considering the high oxidation potential of •OH and the essential role of CeO₂-NR for TOC removal, the effects of adding 50 mM HPO₄²⁻ (reaching a pH of about 9.0) or 50 mM H₂PO₄ (reaching a pH of about 5.0) into the O₃/phenol/CeO₂-NR-300 reaction mixture were evaluated. There is no obvious change in phenol degradation (Fig. 9c), because these anions do not react with O₃ and phenol is predominantly oxidized by O₃. However, both HPO₄²⁻ and H₂PO₄ dramatically reduce the TOC removal, from 61.5% to 30.7% (for HPO₄²⁻) and 24.4% (for H₂PO₄) at 60 min (Fig. 9d). Because HPO₄²⁻ and H₂PO₄ are masking agents of surface OH and Lewis acid sites (metal cations) that are essential for O₃ activation to generate ROS (such as •OH) [10,12], and themselves are also scavengers for •OH [54], the above result reveals •OH is probably the major ROS for TOC

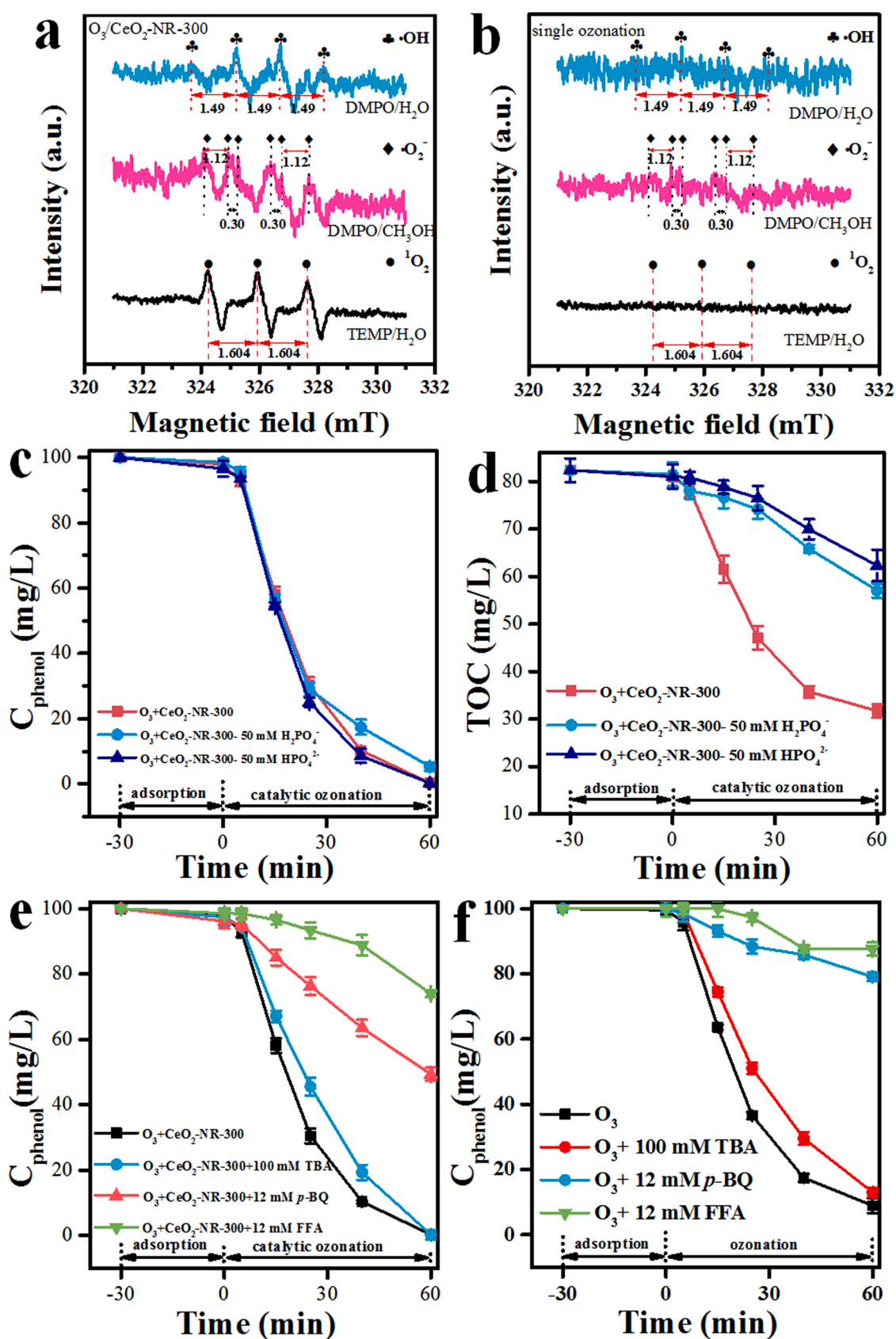


Fig. 9. ESR spectra for catalytic ozonation on $\text{CeO}_2\text{-NR-300}$ (a) and single ozonation (b) in different mixtures, phenol degradation curves (c) and the corresponding TOC removal (d) by catalytic ozonation on $\text{CeO}_2\text{-NR-300}$ with the addition of HPO_4^{2-} and H_2PO_4^- , and the phenol degradation curves for catalytic ozonation on $\text{CeO}_2\text{-NR-300}$ (e) and single ozonation (f) with the addition of different quenching agents.

removal. Meanwhile, the TOC removal with the presence of HPO_4^{2-} or $\text{H}_2\text{PO}_4^{2-}$ is still better than that of single ozonation (16.9%) (Figs. 9d and 6c). This is probably because $\bullet\text{OH}$ cannot be completely scavenged by the anions and some other ROS, such as $\bullet\text{O}_2^-$ and surface oxygen atom (O^* , 2.43 eV), contributes to TOC removal. In the work of Wang et al. [55], $\bullet\text{O}_2^-$ played a major role for TOC removal. In the work of Zhang et al. [20], TOC removal via the reaction between O^* and adsorbed oxalate was important. Moreover, other common quenching agents were considered. According to literature [2,56], interpretation of the quenching results in HCO processes should be careful because the common quenching agents, such as *p*-BQ and FFA, can also fast react with O_3 . In this work, the effects of adding TBA with $k(\bullet\text{OH})$ of $6 \times 10^8 \text{ L}/(\text{mol}\cdot\text{s})$ and $k(\text{O}_3)$ of $3 \times 10^{-3} \text{ L}/(\text{mol}\cdot\text{s})$ [2], *p*-BQ with $k(\bullet\text{O}_2^-)$ of $9.8 \times 10^8 \text{ L}/(\text{mol}\cdot\text{s})$ and $k(\text{O}_3)$ of $2.5 \times 10^3 \text{ L}/(\text{mol}\cdot\text{s})$ [56], and FFA with $k(^1\text{O}_2)$ of $1.2 \times 10^8 \text{ L}/(\text{mol}\cdot\text{s})$, $k(\bullet\text{OH})$ $1.5 \times 10^{10} \text{ L}/(\text{mol}\cdot\text{s})$ and $k(\text{O}_3)$ of $1.6 \times 10^3 \text{ L}/(\text{mol}\cdot\text{s})$ [2,56], in the catalytic and single ozonation systems were evaluated. In single ozonation, TBA slightly declines the phenol degradation rate, while *p*-BQ and FFA cause huge inhibitions ($> 80\%$) (Fig. 9f). Because phenol itself is mainly oxidized by O_3 , the scavenging effects are mainly attributed to the fast depletion of O_3 by *p*-BQ and FFA although the occurrence of $\bullet\text{OH}$ quenching cannot be excluded. Interestingly, in the HCO process, while TBA results in a similar minor inhibition, *p*-BQ and FFA inhibit the degradation to less degrees compared with the cases in single ozonation (Fig. 9e, f). This is because part of the O_3 remains in the reaction solution and it can still be activated by $\text{CeO}_2\text{-NR-300}$ to generate ROS to degrade phenol even though most O_3 is

consumed by *p*-BQ or FFA. With FFA added, because of the quenching of $\bullet\text{OH}$ and $^1\text{O}_2$, the better phenol degradation in HCO than in single ozonation can be attributed to $\bullet\text{O}_2^-$. Similarly, with *p*-BQ added, because of the quenching of $\bullet\text{O}_2^-$, the better phenol degradation in HCO than in single ozonation can be attributed to $\bullet\text{OH}$ and $^1\text{O}_2$. Therefore, by combining the above results, it can be concluded that $\bullet\text{OH}$, $\bullet\text{O}_2^-$ and $^1\text{O}_2$ can be produced in the HCO process. O_3 is the major oxidant in the initial stage of phenol oxidation. In the deep oxidation stage and TOC removal, $\bullet\text{OH}$ (major) and $\bullet\text{O}_2^-$ play important roles and O^* cannot be ruled out.

3.5. Discussion on the key descriptor and mechanism insight

In previous works on using CeO_2 (and other TMOs) for HCO, efforts have been made to correlate the performances with their properties [5, 18,19,22]. However, establishing a simple but critical descriptor is difficult because many properties (such as surface area, acid-base site, metal valence, OH and OV) of the catalysts are variable and their interplay with the activity is complicated. In order to identify the critical descriptor, the $k_{\text{O}_3\text{-cata}}$ and TOC removal values as performance parameters of $\text{CeO}_2\text{-NR-T}$ were plotted against various physicochemical parameters. The performance parameters cannot be well correlated with the values of surface area, $\text{Ce}^{3+}\%$, OH density, and acid site density (Fig. S10). Most importantly, both the plots of TOC removal (for degradation of all the three different pollutants) and $k_{\text{O}_3\text{-cata}}$ against the $I_{\text{D}}/I_{\text{F}2\text{g}}$ value show positive and linear correlations (Fig. 10). These

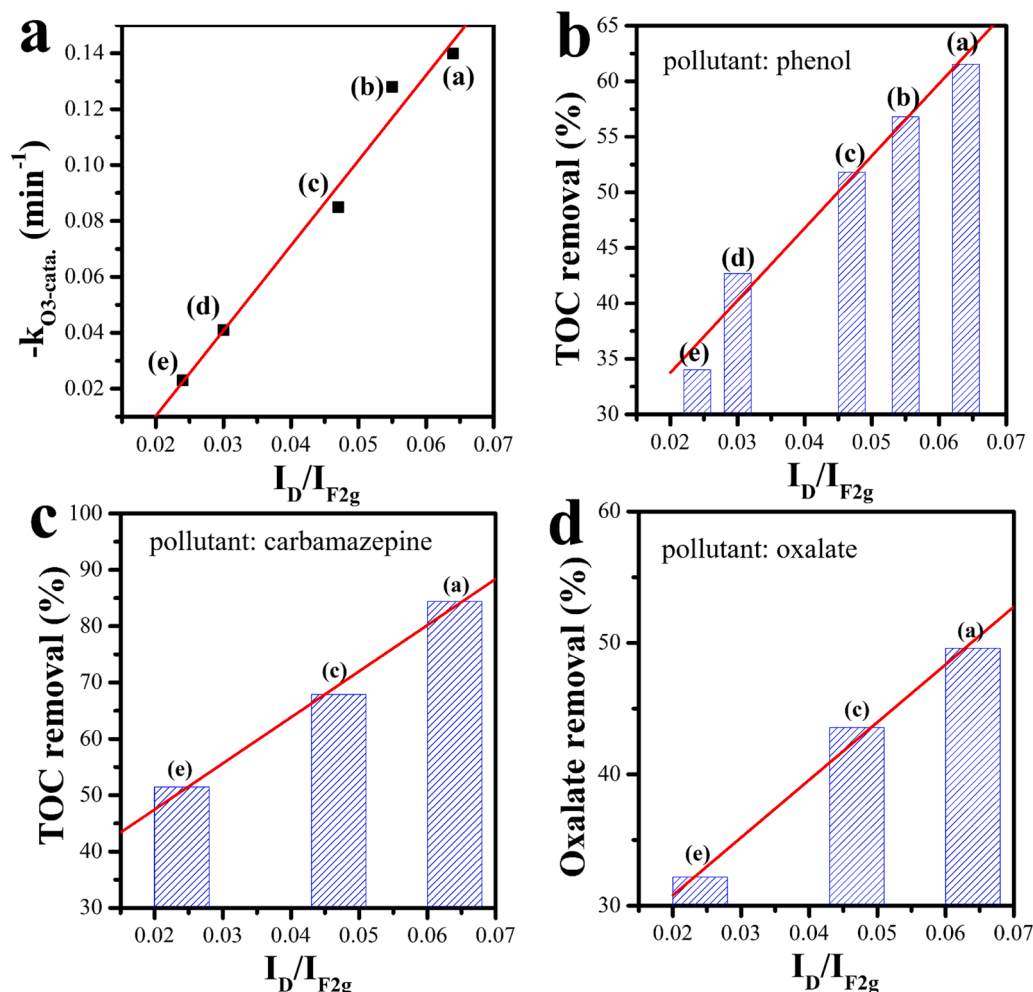


Fig. 10. Linear plots of $-k_{\text{O}_3\text{-cata}}$ (a) and TOC removal at 60 min (b-d) against the $I_{\text{D}}/I_{\text{F}2\text{g}}$ values of the $\text{CeO}_2\text{-NR-T}$ samples calcined at (a) 300, (b) 400, (c) 500, (d) 600, and (e) 700 °C, respectively.

results clearly reveal the Frenkel-type OV of CeO₂ is vital for O₃ activation and TOC removal, and it can be used as the descriptor for the HCO performance of CeO₂-NR-T, which has not been reported before.

DFT calculations were performed to gain some insight on the roles of surface OH and Frenkel-type OV in HCO. Because the main exposed facet of CeO₂-NR is (110), O₃ adsorption models on different sites of CeO₂ (110) were simulated and optimized, and the corresponding adsorption energy and bonding length parameters were calculated (Fig. 11 and Table 2). The O₃ adsorption energies on the Ce atom of bare CeO₂ (110) and OV-CeO₂ (110) surfaces are −0.77 eV and −1.88 eV, respectively (Fig. 11a, b). A very similar difference can be found for O₃ adsorbed on the Ce atom of OH-CeO₂ (110) and OH&OV-CeO₂ (110) surfaces (−0.78 eV and −1.88 eV) (Fig. 11c, d). Meanwhile, the bonding length ($d_{\text{OI-OII}}$) significantly increases at the presence of OV, indicating weakening of the chemical bonds of O₃. Interestingly, by comparing the O₃ adsorption energies between CeO₂ (110) and OH-CeO₂ (110), as well as between OV-CeO₂ (110) and OH&OV-CeO₂ (110), there is almost no difference, indicating OH has little effect on O₃ adsorption on the Ce atoms [10,57]. Indeed, the adsorption energy of O₃ on the OH site of the OH-CeO₂ (110) surface is only −0.24 eV (Fig. 11e). Surprisingly, O₃ adsorption on the OH site of the OH&OV-CeO₂ (110) OH&OV-CeO₂ (110) surfaces is not stable and the OH can be filled into the OV site after optimization (Fig. 11f, g), and the energy changes rocket to −3.29 eV and −3.06 eV for the terminal and penta-ring configurations, respectively. Meanwhile, the bonding lengths of both O_I-O_{II} and O_{II}-O_{III} of adsorbed O₃ are simultaneously and dramatically stretched. These results clearly suggest OV can greatly facilitate the activation of O₃ at both the surface Ce atom and OH site. In addition, O₃ seems to be more preferably activated by the surface OH associated with OV on CeO₂ surfaces.

In-situ ATR-FTIR further experimentally depicted the O₃/CeO₂-NR-300 interactions (Fig. 12). In the spectrum of the CeO₂-NR-300/H₂O, characteristic signals of chemisorbed H₂O (3230 and 1630 cm^{−1}) can be observed [58]. By replacing H₂O with D₂O, new peaks (2448, 2391, 2335 and 1206 cm^{−1}) can be identified, and the original peaks from chemically adsorbed H₂O disappear [59]. The signal at 2448 cm^{−1} is assigned to the stretching vibration of CeO-D, while those at 2391, 2335

Table 2

Summary of the O₃ adsorption energy and the corresponding O-O bonding length at the Ce and OH sites of different model surfaces.

Adsorption site	Model	Adsorption energy (eV)	$d_{\text{OI-OII}}$ (Å)	$d_{\text{OII-OIII}}$ (Å)
/	O ₃	/	1.28476 (0)	1.28483 (0)
Ce	O ₃ + CeO ₂ (110)	−0.77	1.36302 (0)	1.29091 (0)
	O ₃ + OV-CeO ₂ (110)	−1.88	1.46765 (0)	1.29120 (0)
	O ₃ + OH-CeO ₂ (110)	−0.78	1.33113 (0)	1.32375 (0)
	O ₃ + OH&OV-CeO ₂ (110)	−1.88	1.40396 (0)	1.30925 (0)
OH	O ₃ + OH-CeO ₂ (110)	−0.24	1.29095 (0)	1.36310 (0)
	O ₃ + OH&OV-CeO ₂ (110) "terminal"	−3.29	1.36294 (0)	1.36118 (0)
	O ₃ + OH&OV-CeO ₂ (110) "penta-ring"	−3.06	1.36955 (0)	1.36224 (0)

and 1206 cm^{−1} to hydrogen-bonded D₂O [46,59,60]. The signals at about 1516, 1319 and 1071 cm^{−1} are originated from carbonate species due to the adsorption of CO₂ in air [61]. With O₃ bubbled into CeO₂-NR-300/D₂O, all the peak intensities increase. Moreover, a new strong peak at about 3393 cm^{−1} appears, which can be attributed to the signal of D₂O. These results clearly suggest O₃ can consume the original OH (CeO-H) of CeO₂-NR-300, so that more Ce sites can be re-exposed to promote the adsorption and dissociation of D₂O to form CeO-D [62]. In addition, the catalyst/O₃ interactions can bring about more chemisorbed D₂O (hydrogen-bonded with CeO-D) at the surface of CeO₂-NR-300 [46,63]. Because the formation of CeO-D and chemisorbed D₂O is related with the interactions of O₃ with the CeO-H and the Lewis acid sites [59,60,63], it can be deduced both Ce and OH sites are important for O₃ activation, in agreement with the DFT calculation results.

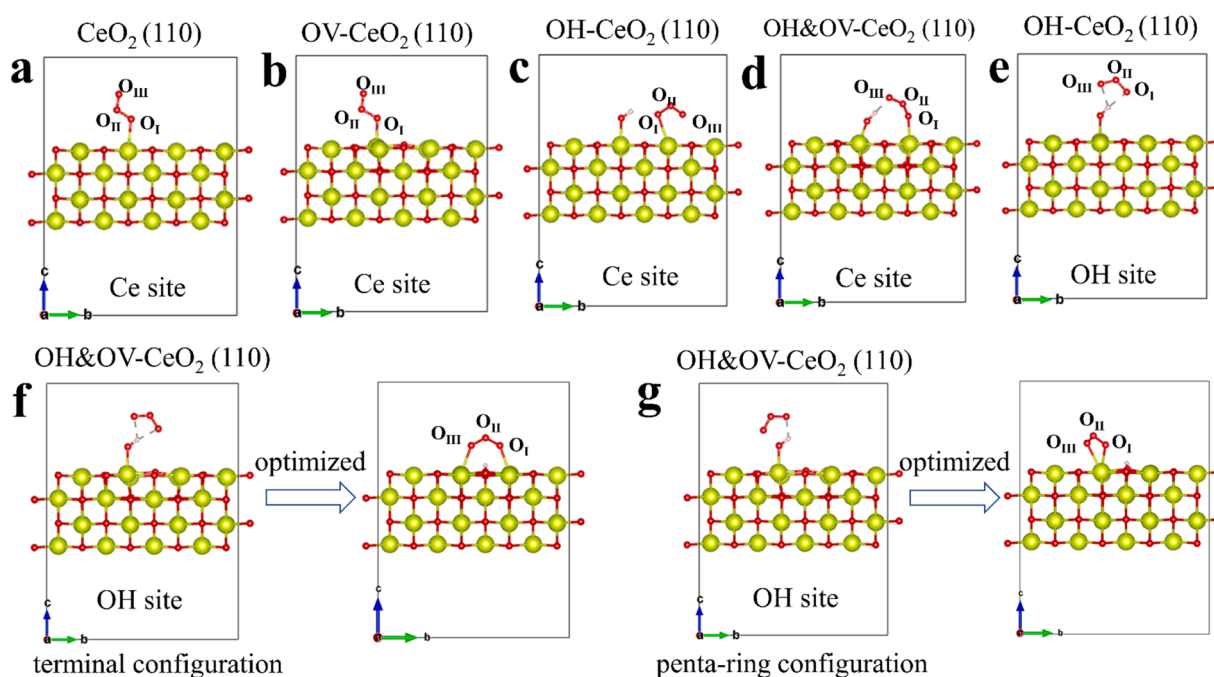


Fig. 11. DFT simulated models for of O₃ adsorption on different sites at CeO₂ (110) surfaces: bare Ce site (a), Ce site with adjacent OV (b), Ce site with adjacent OH (c), Ce site with both adjacent OH and OV (d), OH site via hydrogen bonding (e), and OH site with adjacent OV in the "terminal" (f) and "penta-ring" (g) configurations, respectively. Images (a-e) are optimized after simulation, while (f) and (g) show the initial and optimized models.

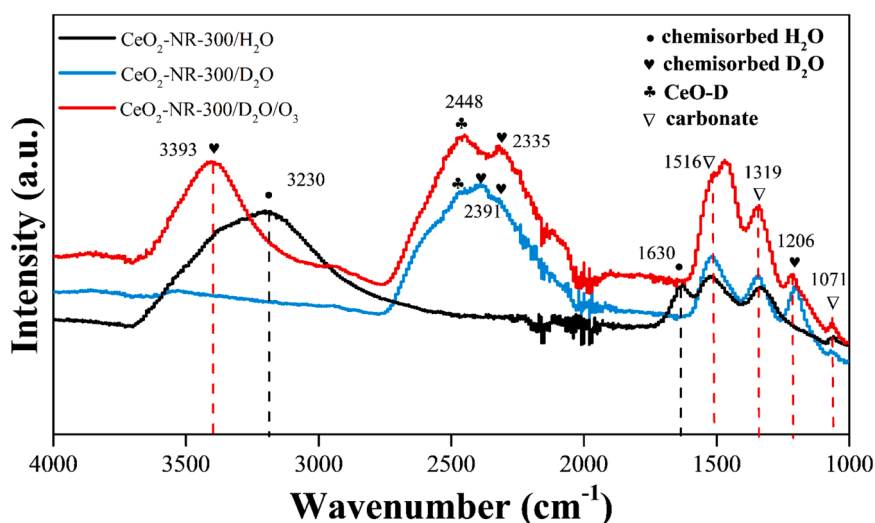


Fig. 12. In-situ ATR-FTIR spectra of CeO₂-NR-300 suspended in H₂O, in D₂O and in O₃-bubbled D₂O.

Finally, the HCO mechanism on CeO₂-NR-T by separating the stages of phenol oxidation and TOC removal is proposed (Fig. 13). First, there are several possible routes for phenol oxidation (Fig. S11). The surface area and the densities of OH, acid site and OV, which significantly influence the adsorption of O₃ and phenol, are all different for CeO₂-NR-T, but their phenol degradation rates are almost the same and close to that of single ozonation. Therefore, phenol oxidation is dominated by direct reaction with O₃ in bulk solution. This is also applicable for the catalytic ozonation of other pollutants (such as CBZ) which have high reaction affinity with O₃. Subsequently, the second stage is the deep oxidation of the intermediates. The direct oxidation of phenol by O₃ can generate a series of intermediates, such as oxalic acid and oxalate ions, which can hardly be further oxidized by O₃ [45]. The deep oxidation of these substances relies on the ROS generated from the adsorbed O₃ at the active sites of CeO₂. Because the chain reactions producing ROS have very high rate constants, the surface activation of O₃ should be the

rate-limiting step for TOC removal [2,54]. The higher the active site density is, the faster the adsorbed O₃ can be activated and the better the TOC removal is. The active sites are directly linked with Frenkel-type OV. The activation of O₃ on both the Ce atom and OH site associated with OV can be greatly promoted, leading to accelerated O₃ decomposition and ROS generation for TOC removal. The generated ROS may include •OH, •O₂⁻, ¹O₂ and O*. The generation of these ROS is complicated but two general paths can be deduced. The first one is the activation of O₃ at the Ce atom of OV-CeO₂ (110) and OV&OH-CeO₂ (110) surfaces to produce O*, •O₂⁻ and ¹O₂ (Eqs. (8)–(10)). This is probably similar to the prior research that Al³⁺-OH [14] and Zn²⁺-OH [64] can promote the production of ROS by activating O₃ without metal valence change. The second one is the activation of O₃ via the OH site of the OV&OH-CeO₂ (110) surfaces to produce •OH and •O₂⁻ (Eqs. (11)–(15)). This reaction process is associated with electron transfer and redox cycling of Ce³⁺/Ce⁴⁺ and O_{latt}/OV. In this case, the ROS reaction path is

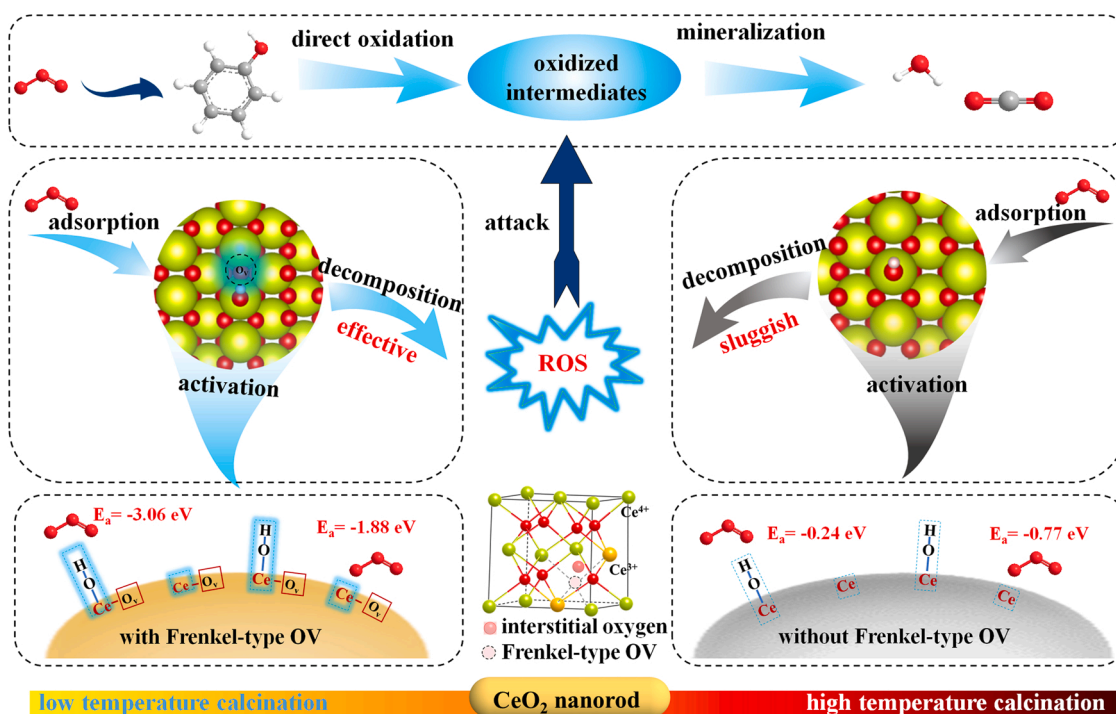
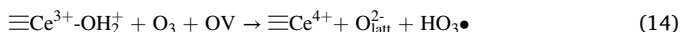
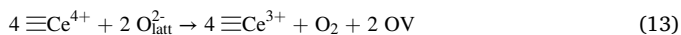
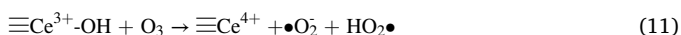
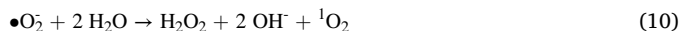
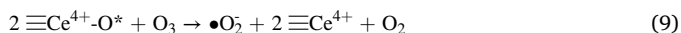


Fig. 13. Schematic representation of the catalytic ozonation mechanism for phenol degradation on CeO₂-NR-T with and without Frenkel-type OV.

accompanied by the conversion of Ce^{3+} to Ce^{4+} and the disappearance of OV. Subsequently, migration of O_{latt} can trigger the redox of $\text{O}_{\text{latt}}/\text{OV}$ to re-generate Ce^{3+} and OV [51,65]. As a result, the chemical state of the catalyst is stable over the HCO process as revealed by the XPS results (Fig. 8c, d).



4. Conclusion

In summary, we presented an effective calcination strategy to modulate the properties of CeO_2 NRs. The representative material showed excellent performance in HCO for abatement of three pollutants (phenol, CBZ and oxalate) with fast degradation, high TOC removal (50–85%), good stability and wide pH (3.5–12) applicability. For the first time, we presented Frenkel-type OV of CeO_2 NRs was the critical descriptor of their O_3 decomposition kinetics and TOC removal. During calcination of the CeO_2 NRs, severe sintering occurred at $\geq 600^\circ\text{C}$, causing fast decline of surface area and elimination of OH and acid-base sites. Frenkel-type OV decreased linearly with the increase of temperature. The contact between calcined CeO_2 NRs and water could re-generate surface OH. Phenol and CBZ could be fast degraded by single ozonation in bulk solution and the CeO_2 NRs induced only slight improvements. The TOC removal for oxalate and the intermediates from phenol and CBZ was boosted using the CeO_2 NRs. The best TOC removal on the CeO_2 NRs was achieved at a pH close to the pH_{pzc} . Their TOC removal rates varied with the surface area and the densities of OH and acid-base sites, but clear correlations could not be established. Frenkel-type OV was linearly correlated with the O_3 decomposition kinetics and TOC removal for degradation of the three pollutants. DFT calculations and in-situ ATR-FTIR studies revealed the activation of O_3 on both the surface Ce atom and OH site of the CeO_2 NRs with the presence of OV was greatly promoted to accelerate O_3 decomposition. Several types of ROS ($\bullet\text{OH}$, $\bullet\text{O}_2^-$, ${}^1\text{O}_2$ and O^*) could be generated through various proposed pathways. Quenching and ESR results revealed $\bullet\text{OH}$ was the major ROS for TOC removal and the roles of $\bullet\text{O}_2^-$ and O^* could not be ignored. This study highlights the importance of Frenkel-type OV in CeO_2 NRs and the mechanism in HCO. It would provide useful hints for designing efficient TMOs and interpreting and predicting their performances in HCO for the abatement of different pollutants in wastewaters.

CRediT authorship contribution statement

Lei Wu led the conduction of experiments and data analysis. Jiaren Wang, Chenyu Yang, Xingmin Gao and Yan Fang contributed to conducting experiments and data analysis. Zhangxiong Wu conceived the idea and led the project. Xiaoning Wang, Winston Duo Wu and Zhangxiong Wu co-supervised the project and acquired the funding. Lei Wu and Zhangxiong Wu led the writing and editing of the manuscript draft. All the other authors contributed to reviewing and editing the manuscript.

Declaration of Competing Interest

The authors declare that they have no known competing financial interests or personal relationships that could have appeared to influence the work reported in this paper.

Data availability

Data will be made available on request.

Acknowledgments

This work was supported by the National Natural Science Foundation of China (21875153, 21878197 and 21906111), and the Suzhou Municipal Science and Technology Bureau (SYG201637, SYG201810 and SNG2022053), and the Priority Academic Program Development (PAPD) of Jiangsu Higher Education Institutions.

Appendix A. Supporting information

Supplementary data associated with this article can be found in the online version at doi:10.1016/j.apcatb.2022.122152.

References

- [1] J. Wang, H. Chen, Catalytic ozonation for water and wastewater treatment: Recent advances and perspective, *Sci. Total Environ.* 704 (2020), 135249.
- [2] G. Yu, Y. Wang, H. Cao, H. Zhao, Y. Xie, Reactive oxygen species and catalytic active sites in heterogeneous catalytic ozonation for water purification, *Environ. Sci. Technol.* 54 (2020) 5931–5946.
- [3] V.I. Parvulescu, F. Epron, H. Garcia, P. Granger, Recent progress and prospects in catalytic water treatment, *Chem. Rev.* 122 (2022) 2981–3121.
- [4] J. Wang, Z. Bai, Fe-based catalysts for heterogeneous catalytic ozonation of emerging contaminants in water and wastewater, *Chem. Eng. J.* 312 (2017) 79–98.
- [5] S. Afzal, X. Qian, S. Lu, Catalytic performance and an insight into the mechanism of CeO_2 nanocrystals with different exposed facets in catalytic ozonation of p-nitrophenol, *Appl. Catal. B-Environ.* 248 (2019) 526–537.
- [6] P. Li, S. Zhan, L. Yao, Y. Xiong, S. Tian, Highly porous alpha- MnO_2 nanorods with enhanced defect accessibility for efficient catalytic ozonation of refractory pollutants, *J. Hazard. Mater.* 437 (2022), 129235–129235.
- [7] T. Shen, W. Su, Q. Yang, J. Ni, S. Tong, Synergetic mechanism for basic and acid sites of MgM_xO_y ($M = \text{Fe}, \text{Mn}$) double oxides in catalytic ozonation of p-hydroxybenzoic acid and acetic acid, *Appl. Catal. B-Environ.* 279 (2020), 119346.
- [8] C. Shan, Y. Xu, M. Hua, M. Gu, Z. Yang, P. Wang, Z. Lu, W. Zhang, B. Pan, Mesoporous Ce-Ti-Zr ternary oxide millispheres for efficient catalytic ozonation in bubble column, *Chem. Eng. J.* 338 (2018) 261–270.
- [9] S. Afzal, X. Qian, J. Zhang, High surface area mesoporous nanocast LaMO_3 ($M = \text{Mn}, \text{Fe}$) perovskites for efficient catalytic ozonation and an insight into probable catalytic mechanism, *Appl. Catal. B-Environ.* 206 (2017) 692–703.
- [10] Y. Wang, L. Chen, H. Cao, Z. Chi, C. Chen, X. Duan, Y. Xie, F. Qi, W. Song, J. Liu, S. Wang, Role of oxygen vacancies and Mn sites in hierarchical $\text{Mn}_2\text{O}_3/\text{LaMnO}_3$ delta perovskite composites for aqueous organic pollutants decontamination, *Appl. Catal. B-Environ.* 245 (2019) 546–554.
- [11] S. Li, X. Li, H. Wu, X. Sun, F. Gu, L. Zhang, H. He, L. Li, Mechanism of Synergistic Effect on Electron Transfer over Co-Ce/MCM-48 during Ozonation of Pharmaceuticals in Water, *ACS Appl. Mater. Interfaces* 11 (2019) 23957–23971.
- [12] T. Zhang, C. Li, J. Ma, H. Tian, Z. Qiang, Surface hydroxyl groups of synthetic alpha- FeOOH in promoting-OH generation from aqueous ozone: Property and activity relationship, *Appl. Catal. B-Environ.* 82 (2008) 131–137.
- [13] L. Zhao, Z. Sun, J. Ma, Novel relationship between hydroxyl radical initiation and surface group of ceramic honeycomb supported metals for the catalytic ozonation of nitrobenzene in aqueous solution, *Environ. Sci. Technol.* 43 (2009) 4157–4163.
- [14] J. Bing, C. Hu, Y. Nie, M. Yang, J. Qu, Mechanism of Catalytic Ozonation in $\text{Fe}_2\text{O}_3/\text{Al}_2\text{O}_3$ @SBA-15 Aqueous Suspension for Destruction of Ibuprofen, *Environ. Sci. Technol.* 49 (2015) 1690–1697.
- [15] Y.Y. Ma, W. Gao, Z.Y. Zhang, Z.M. Tian, Y.X. Liu, J.C. Ho, Y.Q. Qu, Regulating the surface of nanoceria and its applications in heterogeneous catalysis, *Surf. Sci. Rep.* 73 (2018) 1–36.
- [16] B. Huang, R. Gillen, J. Robertson, Study of CeO_2 and its native defects by density functional theory with repulsive potential, *J. Phys. Chem. C* 118 (2014) 24248–24256.
- [17] T. Zhang, W. Chen, J. Ma, Z. Qiang, Minimizing bromate formation with cerium dioxide during ozonation of bromide-containing water, *Water Res.* 42 (2008) 3651–3658.
- [18] C.A. Orge, J.J.M. Orfao, M.F.R. Pereira, A.M. Duarte de Farias, R.C. Rabelo Neto, M.A. Fraga, Ozonation of model organic compounds catalysed by nanostructured cerium oxides, *Appl. Catal. B-Environ.* 103 (2011) 190–199.

- [19] L.-H. Zhang, J. Zhou, Z.-Q. Liu, J.-B. Guo, Mesoporous CeO₂ Catalyst Synthesized by Using Cellulose as Template for the Ozonation of Phenol, *Ozone-Sci. Eng.* 41 (2019) 166–174.
- [20] T. Zhang, W. Li, J.-P. Croue, Catalytic Ozonation of Oxalate with a Cerium Supported Palladium Oxide: An Efficient Degradation Not Relying on Hydroxyl Radical Oxidation, *Environ. Sci. Technol.* 45 (2011) 9339–9346.
- [21] J. Feng, X. Zhang, J. Fu, H. Chen, Catalytic ozonation of oxalic acid over rod-like ceria coated on activated carbon, *Catal. Commun.* 110 (2018) 28–32.
- [22] M.F. Pinheiro da Silva, L.S. Soeira, K.R.P. Daghestanli, T.S. Martins, I.M. Cuccovia, R.S. Freire, P.C. Isolani, CeO₂-catalyzed ozonation of phenol, *J. Therm. Anal. Calorim.* 102 (2010) 907–913.
- [23] H.-X. Mai, L.-D. Sun, Y.-W. Zhang, R. Si, W. Feng, H.-P. Zhang, H.-C. Liu, C.-H. Yan, Shape-selective synthesis and oxygen storage behavior of ceria nanopolyhedra, nanorods, and nanocubes, *J. Phys. Chem. B* 109 (2005) 24380–24385.
- [24] G. Kresse, J. Furthmüller, Efficiency of ab-initio total energy calculations for metals and semiconductors using a plane-wave basis set, *Comput. Mater. Sci.* 6 (1996) 15–50.
- [25] P.E. Blochl, Projector augmented-wave method, *Phys. Rev. B* 50 (1994) 17953–17979.
- [26] J.P. Perdew, J.A. Chevary, S.H. Vosko, K.A. Jackson, M.R. Pederson, D.J. Singh, C. Fiolhais, Atoms, molecules, solids, and surfaces - applications of the generalized gradient approximation for exchange and correlation, *Phys. Rev. B* 46 (1992) 6671–6687.
- [27] A.D. Oyedele, S. Yang, L. Liang, A.A. Puzetzy, K. Wang, J. Zheng, P. Yu, P. R. Pudasaini, A.W. Ghosh, Z. Liu, C.M. Rouleau, B.G. Sumpter, M.F. Chisholm, W. Zhou, P.D. Rack, D.B. Geoghegan, K. Xiao, PdSe₂: Pentagonal Two-Dimensional Layers with High Air Stability for Electronics, *J. Am. Chem. Soc.* 139 (2017) 14090–14097.
- [28] C. Loschen, J. Carrasco, K.M. Neyman, F. Illas, First-principles LDA plus U and GGA plus U study of cerium oxides: Dependence on the effective U parameter, *Phys. Rev. B* 75 (2007), 035115.
- [29] Y. Cao, L. Zhao, T. Gutmann, Y. Xu, L. Dong, G. Buntkowsky, F. Gao, Getting Insights into the Influence of Crystal Plane Effect of Shaped Ceria on Its Catalytic Performances, *J. Phys. Chem. C* 122 (2018) 20402–20409.
- [30] Y. Xie, J. Wu, G. Jing, H. Zhang, S. Zeng, X. Tian, X. Zou, J. Wen, H. Su, C.-J. Zhong, P. Cui, Structural origin of high catalytic activity for preferential CO oxidation over CuO/CeO₂ nanocatalysts with different shapes, *Appl. Catal. B: Environ.* 239 (2018) 665–676.
- [31] Z. Yu, X. Gao, Y. Yao, X. Zhang, G.-Q. Bian, W.D. Wu, X.D. Chen, W. Li, C. Selomulya, Z. Wu, D. Zhao, Scalable synthesis of wrinkled mesoporous titania microspheres with uniform large micron sizes for efficient removal of Cr(VI), *J. Mater. Chem. A* 6 (2018) 3954–3966.
- [32] N. Bosio, A. Schaefer, H. Gronbeck, Can oxygen vacancies in ceria surfaces be measured by O1s photoemission spectroscopy? *J. Phys. -Condens. Matter* 34 (2022), 174004.
- [33] B. Chen, Y. Ma, L. Ding, L. Xu, Z. Wu, Q. Yuan, W. Huang, Reactivity of Hydroxyls and Water on a CeO₂(111) Thin Film Surface: The Role of Oxygen Vacancy, *J. Phys. Chem. C* 117 (2013) 5800–5810.
- [34] F. Dvůřák, L. Szabová, V. Johánek, M. Farnesi Camellone, V. Stetsovych, M. Vorokhta, A. Tovt, T. Skála, I. Matolínová, Y. Tateyama, J. Mysliveček, S. Fabris, V. Matolín, Bulk Hydroxylation and Effective Water Splitting by Highly Reduced Cerium Oxide: The Role of O Vacancy Coordination, *ACS Catal.* 8 (2018) 4354–4363.
- [35] A. Badri, C. Binet, J.C. Lavalley, An FTIR study of surface ceria hydroxy groups during a redox process with H₂, *J. Chem. Soc. -Faraday Trans.* 92 (1996) 4669–4673.
- [36] C. Binet, M. Daturi, J.C. Lavalley, IR study of polycrystalline ceria properties in oxidised and reduced states, *Catal. Today* 50 (1999) 207–225.
- [37] R. Schmitt, A. Nénning, O. Kraynis, R. Korobko, A.I. Frenkel, I. Lubomirsky, S. M. Haile, J.L.M. Rupp, A review of defect structure and chemistry in ceria and its solid solutions, *Chem. Soc. Rev.* 49 (2020) 554–592.
- [38] Y. Lee, G. He, A.J. Akey, R. Si, M. Flytzani-Stephanopoulos, I.P. Herman, Raman Analysis of Mode Softening in Nanoparticle CeO_{2-delta} and Au-CeO_{2-delta} during CO Oxidation, *J. Am. Chem. Soc.* 133 (2011) 12952–12955.
- [39] Z. Wu, M. Li, J. Howe, H.M. Meyer III, S.H. Overbury, Probing Defect Sites on CeO₂ Nanocrystals with Well-Defined Surface Planes by Raman Spectroscopy and O₂ Adsorption, *Langmuir* 26 (2010) 16595–16606.
- [40] Y. Wang, F. Wang, Q. Song, Q. Xin, S. Xu, J. Xu, Heterogeneous Ceria Catalyst with Water-Tolerant Lewis Acidic Sites for One-Pot Synthesis of 1,3-Diols via Prins Condensation and Hydrolysis Reactions, *J. Am. Chem. Soc.* 135 (2013) 1506–1515.
- [41] L. Zhao, Z. Sun, J. Ma, H. Liu, Enhancement Mechanism of Heterogeneous Catalytic Ozonation by Cordierite-Supported Copper for the Degradation of Nitrobenzene in Aqueous Solution, *Environ. Sci. Technol.* 43 (2009) 2047–2053.
- [42] D.R. Mullins, P.M. Albrecht, T.-L. Chen, F.C. Calaza, M.D. Biegalski, H.M. Christen, S.H. Overbury, Water Dissociation on CeO₂(100) and CeO₂(111) Thin Films, *J. Phys. Chem. C* 116 (2012) 19419–19428.
- [43] H. Tamura, A. Tanaka, K.-Y. Mita, R. Furuchi, Surface hydroxyl site densities on metal oxides as a measure for the ion-exchange capacity, *J. Colloid Interface Sci.* 209 (1999) 225–231.
- [44] H.P. Boehm, Acidic and basic properties of hydroxylated metal oxide surfaces, *Discuss. Faraday Soc.* 52 (1971) 254–275.
- [45] L.F. Liotta, M. Gruttadauria, G. Di Carlo, G. Perrini, V. Librando, Heterogeneous catalytic degradation of phenolic substrates: Catalysts activity, *J. Hazard. Mater.* 162 (2009) 588–606.
- [46] H. Zhao, Y.M. Dong, P.P. Jiang, G.L. Wang, J.J. Zhang, K. Li, An insight into the kinetics and interface sensitivity for catalytic ozonation: the case of nano-sized NiFe₂O₄, *Catal. Sci. Technol.* 4 (2014) 494–501.
- [47] S.T. Oyama, Chemical and catalytic properties of ozone, *Catal. Rev.* 42 (2000) 279–322.
- [48] J. Wang, X. Quan, S. Chen, H. Yu, G. Liu, Enhanced catalytic ozonation by highly dispersed CeO₂ on carbon nanotubes for mineralization of organic pollutants, *J. Hazard. Mater.* 368 (2019) 621–629.
- [49] L. Chen, J. Duan, P. Du, W. Sun, B. Lai, W. Liu, Accurate identification of radicals by in-situ electron paramagnetic resonance in ultraviolet-based homogenous advanced oxidation processes, *Water Res.* 221 (2022), 118747–118747.
- [50] L. Wang, X. Lan, W. Peng, Z. Wang, Uncertainty and misinterpretation over identification, quantification and transformation of reactive species generated in catalytic oxidation processes: A review, *J. Hazard. Mater.* 408 (2021), 124436.
- [51] C. Fang, X. Gao, X. Zhang, J. Zhu, S.-P. Sun, X. Wang, W.D. Wu, Z. Wu, Facile synthesis of alkaline-earth metal manganites for the efficient degradation of phenolic compounds via catalytic ozonation and evaluation of the reaction mechanism, *J. Colloid Interface Sci.* 551 (2019) 164–176.
- [52] H. Chen, C. Fang, X. Gao, G. Jiang, X. Wang, S.-P. Sun, W.D. Wu, Z. Wu, Sintering- and oxidation-resistant ultrasmall Cu(I)/Cu(II) oxides supported on defect-rich mesoporous alumina microspheres boosting catalytic ozonation, *J. Colloid Interface Sci.* 581 (2021) 964–978.
- [53] Y. Sheng, I.A. Abreu, D.E. Cabelli, M.J. Maroney, A.-F. Miller, M. Teixeira, J. S. Valentine, Superoxide Dismutases and Superoxide Reductases, *Chem. Rev.* 114 (2014) 3854–3918.
- [54] B. Kasprzyk-Hordern, M. Ziślek, J. Nawrocki, Catalytic ozonation and methods of enhancing molecular ozone reactions in water treatment, *Appl. Catal. B: Environ.* 46 (2003) 639–669.
- [55] Y. Wang, Y. Xie, H. Sun, J. Xiao, H. Cao, S. Wang, Hierarchical shape-controlled mixed-valence calcium manganites for catalytic ozonation of aqueous phenolic compounds, *Catal. Sci. Technol.* 6 (2016) 2918–2929.
- [56] Y. Guo, J. Long, J. Huang, G. Yu, Y. Wang, Can the commonly used quenching method really evaluate the role of reactive oxygen species in pollutant abatement during catalytic ozonation? *Water Res.* 215 (2022), 118275.
- [57] X. Chen, H. Yang, C. Au, S. Tian, Y. Xiong, Y. Chang, Efficiency and mechanism of pollutant degradation and bromate inhibition by faceted CeO₂ catalyzed ozonation: Experimental and theoretical study, *Chem. Eng. J.* 390 (2020), 124480.
- [58] S.S. Sable, P.P. Ghute, D. Fakhraee, R.B. Mane, C.V. Rode, F. Medina, S. Contreras, Catalytic ozonation of clofibric acid over copper-based catalysts: In situ ATR-IR studies, *Appl. Catal. B-Environ.* 209 (2017) 523–529.
- [59] A.H. Lv, C. Hu, Y.L. Nie, J.H. Qu, Catalytic ozonation of toxic pollutants over magnetic cobalt and manganese co-doped gamma-Fe₂O₃, *Appl. Catal. B-Environ.* 100 (2010) 62–67.
- [60] W.W. Li, Z.M. Qiang, T. Zhang, F.L. Cao, Kinetics and mechanism of pyruvic acid degradation by ozone in the presence of PdO/CeO₂, *Appl. Catal. B-Environ.* 113 (2012) 290–295.
- [61] C. Li, Y. Sakata, T. Arai, K. Domen, K. Maruya, T. Onishi, Carbon-monoxide and carbon-dioxide adsorption on cerium oxide studied by fourier-transform infrared-spectroscopy.1. formation of carbonate species on dehydroxylated CeO₂ at room-temperature, *J. Chem. Soc. -Faraday Trans. I* 85 (1989) 929–943.
- [62] L. Yang, C. Hu, Y. Nie, J. Qu, Catalytic ozonation of selected pharmaceuticals over mesoporous alumina-supported manganese oxide, *Environ. Sci. Technol.* 43 (2009) 2525–2529.
- [63] L. Yang, C. Hu, Y.L. Nie, J.H. Qu, Surface acidity and reactivity of beta-FeOOH/Al₂O₃ for pharmaceuticals degradation with ozone: In situ ATR-FTIR studies, *Appl. Catal. B-Environ.* 97 (2010) 340–346.
- [64] S. Zhang, X. Quan, D. Wang, Catalytic ozonation in arrayed zinc oxide nanotubes as highly efficient mini-column catalyst reactors (MCRs): augmentation of hydroxyl radical exposure, *Environ. Sci. Technol.* 52 (2018) 8701–8711.
- [65] S. Agarwal, X. Zhu, E.J.M. Hensen, B.L. Mojet, L. Lefferts, Surface-dependence of defect chemistry of nanostructured ceria, *J. Phys. Chem. C* 119 (2015) 12423–12433.